Defects, dopants and Li-ion diffusion in Li2SiO3

Kuganathan, N, Tsoukalas, LH & Chroneos, A

DOI 10.1016/j.ssi.2019.02.019
ISSN 0167-2738

Publisher: Elsevier

Defects, Dopants and Li-ion diffusion in Li_2SiO_3

N. Kuganathan[1,2], L.H. Tsoukalas,[3] and A. Chroneos[2]

[1]Department of Materials, Imperial College London, London, SW7 2AZ, United Kingdom

[2]Faculty of Engineering, Environment and Computing, Coventry University, Priory Street, Coventry CV1 5FB, United Kingdom

[3]School of Nuclear Engineering, Purdue University, West Lafayette, IN, USA

ABSTRACT

Lithium metasilicate, Li_2SiO_3, attracts considerable interest for the development of solid breeding blanket material in fusion reactors and solid electrolyte material in lithium ion batteries. Atomistic simulations are employed to study defect processes, dopant behaviour and lithium ion migration in Li_2SiO_3. The vacancy assisted long range Li is along the *bc* plane with the lower activation energy of 0.21 eV suggesting that high ionic conductivity would be observed in this material. The most thermodynamically favourable intrinsic defect type is Li Frenkel (1.66 eV/defect) suggesting that this defect process will ensure the formation of Li vacancies required for Li ion diffusion. Subvalent doping by Al^{3+} on Si site can increase the Li content in Li_2SiO_3, however, experimental verification is required. The favourable isovalent dopant on the Si site is calculated to be Ge^{4+}.

Keywords: Li_2SiO_3; Defects; Li diffusion; Dopants

1. Introduction

Lithium-based ceramics have gained considerable attention in the diverse field of nuclear fusion reactors and lithium ion batteries [1-7]. A Li-based ceramic that has been considered by the community is Li_2SiO_3 [8-12]. In particular, it is a candidate material for the breeder blanket material for future fusion reactors and as an electrolyte material for Li-ion batteries [8-12].

The breeder blanket region is an important area of the fusion reactor as it is behind the plasma-facing first wall. Its function is to convert neutron energy to heat, protect the magnets from irradiation (neutron and gamma) and produce tritium [13,14]. Candidate materials for the breeder blanket should have high lithium density, low chemical reactivity and high melting temperatures.

Li-ion battery are gaining importance due to their application as power sources for consumer electronics and electric cars [15-17]. The principle design criteria for Li-based ceramics for the cathode are low cost, high density of Li, low, environmental impact, high abundance, and fast Li-ion diffusion.

Li_2SiO_3 satisfies many of the criteria for application as an electrolyte material in Li-ion batteries and as a breeder blanket material for future fusion reactors [8-12]. In previous theoretical studies electronic and physical properties of Li_2SiO_3 were calculated [18,19]. Atomistic simulations can provide a complementary view to experiment for the understanding of the defect chemistry and diffusion energetics in Li-based ceramics. Here we have used computational modelling to study the Li-diffusion, intrinsic defect processes and the impact of doping (trivalent and tetravalent) on the defect processes in Li_2SiO_3.

2. Methodology

All calculations were performed using the GULP code [20], which is based on the classical Born model of ionic crystals. The long-range (i.e. Coulombic) ionic interactions and short-range repulsive forces (i.e. electron-electron repulsion and van der Waals interactions) were considered. The Buckingham potentials (refer to Table 1, [21-26]) were used to model short-range repulsive forces. The simulation boxes and ionic positions were relaxed using the Broyden-Fletcher-Goldfarb-Shanno (BFGS) algorithm [27]. A gradient norm of 0.001 eV/Å was used to converge all structures. The Mott-Littleton method [28] was employed to model the point defects and migrating atoms. In this method two concentric spherical regions are constructed and in the inner spherical region (>700 ions) ions are relaxed explicitly. As the current simulations are within a full charge model with dilute limit defect enthalpies are expected to be overestimated. Nevertheless, relative energies and trends will be consistent.

From a thermodynamic viewpoint the defect parameters (for example migration and

formation energies) can be defined via the comparison of the real (defective) crystal to an isobaric or isochoric ideal (non-defective) crystal. These sets of defect formation parameters can be interconnected through thermodynamic relations as discussed in previous studies [29,30]. Here the atomic scale calculations correspond to the isobaric parameters for the migration and formation processes [31,32].

3. Results and discussion

3.1 Li_2SiO_3 crystal structure

Li_2SiO_3 crystallizes into an orthorhombic phase (space group $Cmc2_1$) at ambient pressure and temperature (refer to Figure 1) [33]. Experimentally observed lattice parameters are: a=9.396 Å, b=5.396 Å and c=4.661 Å [33]. Its crystal structure consists of one type of Li atoms (Wyckoff position: 8b), one type of Si atoms (Wyckoff position: 4a) and two types of O atoms (Wyckoff positions: 4a and 8b). Both Li and Si form corner sharing tetrahedral units with adjacent O atoms as shown in the Figure 1. Energy minimisation calculation was performed on the experimental crystal structure to obtain the equilibrium lattice constants. There is an excellent agreement between the experimental and calculated lattice constants as reported in Table 2.

3.2. Intrinsic defect processes

We calculated the isolated vacancy, interstitial and anti-site defect formation energies as the electrochemical behaviour of Li_2SiO_3 can be studied from the energetics of intrinsic defect processes. Here we use Kröger-Vink notation [34] to represent the Frenkel, Schottky and Anti-site intrinsic defect reactions as shown in equations 1-7.

$$\text{Li Frenkel: } \mathrm{Li}_{\mathrm{Li}}^{\mathrm{X}} \rightarrow V_{\mathrm{Li}}' + \mathrm{Li}_{\mathrm{i}}^{\bullet} \quad (1)$$

$$\text{O Frenkel: } \mathrm{O}_{\mathrm{O}}^{\mathrm{X}} \rightarrow V_{\mathrm{O}}^{\bullet\bullet} + \mathrm{O}_{\mathrm{i}}'' \quad (2)$$

$$\text{Si Frenkel: } V_{\mathrm{Si}}^{\mathrm{X}} \rightarrow V_{\mathrm{Si}}'''' + \mathrm{Si}_{\mathrm{i}}^{\bullet\bullet\bullet\bullet} \quad (3)$$

$$\text{Schottky: } 2\,\mathrm{Li}_{\mathrm{Li}}^{\mathrm{X}} + \mathrm{Si}_{\mathrm{Si}}^{\mathrm{X}} + 3\,\mathrm{O}_{\mathrm{O}}^{\mathrm{X}} \rightarrow 2\,V_{\mathrm{Li}}' + V_{\mathrm{Si}}'''' + 3\,V_{\mathrm{O}}^{\bullet\bullet} + \mathrm{Li_2SiO_3} \quad (4)$$

$$\text{Li}_2\text{O Schottky: } 2\,\mathrm{Li}_{\mathrm{Li}}^{\mathrm{X}} + \mathrm{O}_{\mathrm{O}}^{\mathrm{X}} \rightarrow 2\,V_{\mathrm{Li}}' + V_{\mathrm{O}}^{\bullet\bullet} + \mathrm{Li_2O} \quad (5)$$

$$\text{Li/Si antisite (isolated): } \mathrm{Li}_{\mathrm{Li}}^{\mathrm{X}} + \mathrm{Si}_{\mathrm{Si}}^{\mathrm{X}} \rightarrow \mathrm{Li}_{\mathrm{Si}}''' + \mathrm{Si}_{\mathrm{Li}}^{\bullet\bullet\bullet} \quad (6)$$

$$\text{Li/Si antisite (cluster): } \mathrm{Li}_{\mathrm{Li}}^{\mathrm{X}} + \mathrm{Si}_{\mathrm{Si}}^{\mathrm{X}} \rightarrow \{\mathrm{Li}_{\mathrm{Si}}''' : \mathrm{Si}_{\mathrm{Li}}^{\bullet\bullet\bullet}\}^{\mathrm{X}} \quad (7)$$

Reaction energies for these intrinsic defect processes are reported in Figure 2. The most favourable intrinsic defect process is calculated to be the Li Frenkel. The formation energies for the other Frenkel and Schottky defects is highly endoergic suggesting that they are

unlikely to take place at operating temperatures. The Li-Si anti-site is calculated to be the second most favourable defect process suggesting that a small percentage of Li on Si sites (Li_{Si}''') and Si on Li sites ($Si_{Li}^{\bullet\bullet\bullet}$) would be observed particularly at high temperatures. In previous experimental and theoretical studies, this defect has been reported during the preparation of as-prepared material and cycling [3,21,35-46]. The Li_2O Schottky-like reaction (relation 5) is 3.24 eV per defect. The Li_2O Schottky-like reaction (relation 5) is calculated to be 3.24 eV per defect. This reaction would lead to the formation of further V_{Li}' and $V_O^{\bullet\bullet}$ but at high temperatures.

3.3. Lithium ion diffusion

Here we construct different possible diffusion paths responsible for lithium ion migration. Classical pair-potential method has the ability to provide a detailed information on various possible Li ion diffusion paths, which are difficult to determine experimentally. A promising high-rate battery material should exhibit lower activation energies for Li ion diffusion. Four different local Li hops (refer to Figure 3) were identified for the Li vacancy migration. The migration energies and their corresponding Li-Li separation are reported in Table 3. The energy profile diagrams for activation energies are shown in Figure 4. Four possible long-range paths consisting of local Li hops with lower overall activation energies were identified (refer to Table 4). The first long range path (along *bc* plane) exhibits a zig-zag pattern (A→A→A→A) with overall activation energy of 0.21 eV. The second path connects local hops A and B forming another zig-zag pattern (B→A→B→A) with overall activation energy of 0.44 eV. The third long range path also lies in the *bc* plane but with the Li local hop of C exhibits a distorted zig-zag pattern (C→C→C→C) with overall activation energies of 0.66 eV. In the fourth long-range path (D→C→D→C), the Li ion migrates along *a*- axis with the overall migration energy of 1.26 eV. This is because of the longer Li-Li distance of 3.43 Å. The current simulation reveals that Li ion would diffuse with the lowest overall activation energy of 0.21 eV. This indicates that high ionic conductivity would be observed in Li_2SiO_3. Xiao *et al.* [47] performed high-throughput bond-valence analysis in Li_2SiO_3 and reported that one dimensional Li migration paths occur with the activation energy of 0.58 eV. However, the directions of the paths are unavailable. This activation energy value calculated in their study (0.58 eV) is in agreement with the values calculated in the present study (0.44 eV and 0.66

eV). The current investigation finds there would be another long range Li migration pathway is possible with very low activation energy of 0.21 eV.

3.4. Trivalent doping

Incorporating additional lithium into the as-prepared material would increase the capacity and the applicability of Li_2SiO_3 as a promising material for rechargeable lithium batteries. Here we introduce a possible and efficient engineering strategy to create extra Li by doping trivalent cations on Si sites through creating Li interstitials. This is reminiscent of the case of the superionic conductor β-PbF2 (where anion Frenkel formation process dominates) doped with various alkali metals (e.g. Li, Na), where fluorine vacancies are created for charge compensation [48]. This strategy has been previously applied in Li-ion battery materials and solid-oxide fuel cell materials.

The solution of R_2O_3 (R = Al, Ga, Sc, In, Y, Gd and La) *via* the following process (in Kröger-Vink notation) was considered.

$$R_2O_3 + 2Si_{Si}^{X} + Li_2O \rightarrow 2\,R'_{Si} + 2\,Li_i^{\bullet} + 2\,SiO_2 \qquad (8)$$

The solution enthalpies of R_2O_3 calculated using classical pair-potential method are reported in Figure 5. Our calculations show that the Al^{3+} is the most favourable dopant on the Si site, suggesting that additional lithium can be incorporated in the form of interstitials into Li_2SiO_3 by this synthesis-doping strategy at high temperatures. Experimental study can provide the exact concentration of the composition. Here we predict the possible composition of Al-doped Li_2SiO_3 to be $Li_{2+x}Si_{1-x}Al_xO_3$ (x= 0.0 – 1.0). The second favourable dopant is found to be Ga^{3+} with slightly higher solution enthalpy due to the larger ionic radius of Ga^{3+}than that of Al^{3+}. Solution enthalpy increases gradually with the ionic radius of M^{3+} ions reflecting in the bond lengths and bond angles. Figure 6 shows the optimised lengths and angles of trivalent dopants occupying the Si site and the tetrahedral SiO_4 unit in the relaxed structure of undoped Li_2SiO_3. The highest solution enthalpy is observed for La^{3+}. This is due to the larger ionic radius of La^{3+} is 0.77 Å greater than that of Si^{4+}. Thus the solution enthalpy is high. However, the current solution enthalpy values are large and endoergic suggesting that they are unfavourable.

3.5. Tetravalent doping

We calculate the solution enthalpies for the isovalent dopants (Ge^{4+}, Ti^{4+}, Sn^{4+}, Zr^{4+} and Ce^{4+}) substituted on the Si site. The solution enthalpy was calculated using the following reaction equation:

$$MO_2 + Si_{Si}^{X} \rightarrow M_{Si}^{X} + SiO_2 \quad (9)$$

Favourable solution energy was calculated for Ge^{4+}(see Figure 7). This is due to the ionic radius of Si^{4+} (0.26 Å) which is closer to the ionic radius of Ge^{4+}(0.39 Å). The endoergic solution enthalpy of GeO_2 is due to the strong Si-O bond compared to Ge-O bond. The optimised geometrical parameters (bond lengths and bond angles) are shown in Figure 6. The Ge-O bond lengths and O-Ge-O bond angles are closer to the corresponding Si-O bond lengths and O-Si-O bond angle values respectively. Other dopants show higher solution enthalpies and the trend does not follow a linear pattern. Solution enthalpies for TiO_2 and CeO_2 are highly positive meaning that they are highly unlikely to occur.

4. Conclusions

Using atomistic simulation modelling, we have examined intrinsic defect processes, doping behaviour and Li ion migration pathways with activation energies in Li_2SiO_3. The Li Frenkel is calculated to be the lowest energy process meaning that both Li vacancies and Li interstitials will be predominant at equilibrium. The long range vacancy assisted Li ion migration pathway with lowest activation energy (0.21 eV) is along the *bc* plane with zig-zag pattern indicating that ionic conductivity in Li_2SiO_3 would be high. Solution of R_2O_3 (R = Al, Ga, Sc, In, Y, Gd, La) was considered. It is found that Al^{3+} is the promising dopant to increase the Li content in Li_2SiO_3. The lowest solution enthalpy is observed for GeO_2 suggesting that Ge^{4+} is a candidate isovalent dopant on the Si site. This theoretical prediction requires experimental verification.

Acknowledgements

N.K. and A.C. are grateful for funding from the Lloyd's Register Foundation, a charitable foundation helping to protect life and property by supporting engineering-related education, public engagement and the application of research. Computational facilities and support were provided by the High Performance Computing Centre at Coventry University.

References

1. B.L. Ellis, W.R.M. Makahnouk, Y. Makimura, K. Toghill, L.F. Nazar, Nat. Mater. 6 (2007) 749.
2. S.-I. Nishimura, M. Nakamura, R. Natsui, A. Yamada, J. Am. Chem. Soc. 132 (2010) 13596.
3. A.R. Armstrong, N. Kuganathan, M.S. Islam, P.G. Bruce, J. Am. Chem. Soc. 133 (2011) 13031.

4. C.A.J. Fisher, N. Kuganathan, M.S. Islam, J. Mater. Chem. A 1 (2013) 4207.

5. S. Afyon, M. Wörle, R.A. Nesper, Angew. Chemie Inter. Ed. 52 (2013) 12541.

6. E.E. Jay, M.J.D. Rushton, A. Chroneos, R.W. Grimes, J.A. Kilner, Phys. Chem. Chem. Phys. 17 (2015) 178-183.

7. K.J. Griffith, K.M. Wiaderek, G. Cibin, L.E. Marbella, C.P. Grey, Nature 559 (2018) 556.

8. C.E. Johnson, J. Nucl. Mater. 270 (1999) 212.

9. T. Matsuo, H. Ohno, K. Noda, S. Konishi, H. Yoshida, H. Watanabe, J. Chem. Soc., Faraday Trans. 2, 79 (1983) 1205.

10. F. Lefevre, G. Thevenot, J. Nucl. Mater. 141-143 (1986) 1049.

11. G.N. Greaves, S. Sen, Adv. Phys. 56 (2007) 1.

12. H. Lammert, A. Heuer, Phys. Rev. Lett. 104 (2010) 125901.

13. S.T. Murphy, P. Zeller, A. Chartier, L. Van Brutzel, J. Phys. Chem. C 115 (2011) 21874.

14. J.K. Shultis, R.E. Faw, Fundamentals of nuclear science and engineering, Marcel Dekker, New York, 2002, p. 151.

15. M. Armand, J.M. Tarascon, Nature 451 (2008) 652.

16. P. Simon, Y. Gogotsi, Y. Nature Mater. 7 (2008) 845.

17. J.B. Goodenough, J. Solid State Electrochem. 16 (2012) 2019.

18. T. Tang, P. Chen, W. Luo, D. Luo, Y. Wang, J. Nucl. Mater.420 (2012) 31.

19. S.-G. Ma, Y.-H. Shen, X.-G. Kong, T. Gao, X.-J. Chen, C.-J. Xiao, T.-C. Lu, Mater. Des. 118 (2017) 218.

20. J.D. Gale, A.L. Rohl, Molec. Simul. 29 (2003) 291.

21. N. Kuganathan, M.S. Islam, Chem. Mater. 21 (2009) 5196.

22. L. Minervini, M.O. Zacate, R.W. Grimes, Solid State Ion 116 (1999) 339.; R.W. Grimes, G. Busker, M.A. McCoy, A. Chroneos, J.A. Kilner, S.P. Chen, Ber. Bunden-Ges. Phys. Chem. 101, 1204–1210 (1997).

23. M.A. McCoy, R.W. Grimes, W. Lee, Philos. Mag. A 76 (1997) 1187.

24. Busker, G., Chroneos, A., Grimes, R. W. & Chen, I.-W. Solution mechanisms for dopant oxides in yttria. *J. Am. Ceram. Soc.* 82, 1553-1559 (1999).

25. N. Kuganathan, P. Iyngaran, A. Chroneos, Sci. Rep. 8 (2018) 5832.

26. N. Kuganathan, A. Kordatos, A. Chroneos, Sci. Rep. 8 (2018) 12621.

27. J.D. Gale, J. Chem. Soc. Faraday Trans. 93 (1997) 629.

28. N.F. Mott, M.J. Littleton, Trans. Faraday Soc. 34 (1938) 485.

29. P. Varotsos, Phys. Rev. B 76 (2007) 092106 .

30. P. Varotsos, J. Appl. Phys. 101 (2007) 123503.

31. A. Chroneos and R.V. Vovk, Solid State Ion. 274 (2015) 1-3

32. A. Chroneos, Appl. Phys. Rev. 3 (2016) 041304.

33. H. Völlenkle, Zeitschrift fur Kristallographie - New Crystal Structures 154 (1981) 77.

34 F.A. Kröger, H.J. Vink, in: F. Seitz, D. Turnbull (Eds.), Solid State Physics, Academic Press, 1956, p. 307.+

35. A. Nyten, S. Kamali, L. Haggstrom, T. Gustafsson, J.O. Thomas, J. Mater. Chem. 16 (2006) 2266.

36. D. Ensling, M. Stjerndahl, A. Nyten, T. Gustafsson, J.O. Thomas, J. Mater. Chem. 19 (2009) 82.

37. M. Kempaiah Devaraju, Q. Duc Truong, H. Hyodo, Y. Sasaki, I. Honma, Sci. Rep. 5 (2015) 11041.

38. A. Kordatos, N. Kuganathan, N. Kelaidis, P. Iyngaran, A. Chroneos, Sci. Rep 8 (2018) 6754.

39. N. Kuganathan, A. Chroneos, Sci. Rep 8 (2018) 14669.

40. N. Kuganathan, S. Ganeshalingam, A. Chroneos, Sci. Rep 8 (2018) 8140.

41. N. Kuganathan, A. Kordatos, M.E. Fitzpatrick, R.V. Vovk, A. Chroneos, Solid State Ion 327 (2018) 93.

42. N. Kuganathan, A. Kordatos, S. Anurakavan, P. Iyngaran, A. Chroneos, Mater. Chem. Phys. 25 (2019) 34.

43. V.V. Politaev, A.A. Petrenko, V.B. Nalbandyan, B.S. Medvedev, E.S. Shvetsova, J. Solid State Chem. 180 (2007) 1045.

44. N. Kuganathan, A. Kordatos, A. Chroneos, Sci. Rep. 9 (2019) 550.

45. N. Kuganathan, A. Chroneos, Sci. Rep. 9 (2019) 333.

46. N. Kuganathan, A. Kordatos, N. Kelaidis, A. Chroneos, Sci. Rep. (2019) 2192.

48. R. Xiao, H. Li, L. Chen, J Materiomics 1 (2015) 325.

48. P. Varotsos, Solid State Ionics 179 (2008) 438-441.

Table 1. Interatomic potential parameters used in the atomistic simulations of Li_2SiO_3.

Two-body $[\Phi_{ij}(r_{ij}) = A_{ij}\exp(-r_{ij}/\rho_{ij}) - C_{ij}/r_{ij}^6]$					
Interaction	A / eV	ρ / Å	C / eV·Å^6	Y / e	K / eV·Å^{-2}
$Li^+ - O^{2-}$ [21]	632.1018	0.2906	0.00	1.000	99999
$Si^{4+} - O^{2-}$ [21]	1283.91	0.32052	10.66	4.000	99999
$O^{2-} - O^{2-}$ [21]	22764.30	0.149	27.89	−2.860	74.92
$Al^{3+} - O^{2-}$ [22]	1725.20	0.28971	0.000	3.000	99999
$Sc^{3+} - O^{2-}$ [22]	1575.85	0.3211	0.000	3.000	99999
$In^{3+} - O^{2-}$ [23]	1495.65	0.3327	4.33	3.000	99999
$Y^{3+} - O^{2-}$ [22]	1766.40	0.33849	19.43	3.000	99999
$Gd^{3+} - O^{2-}$ [24]	1885.75	0.3399	20.34	3.000	99999
$La^{3+} - O^{2-}$ [22]	2088.79	0.3460	23.25	3.000	99999
$Ga^{3+} - O^{2-}$ [22]	1625.72	0.3019	0.00	3.000	99999
$Ge^{4+} - O^{2-}$ [25]	1497.3996	0.325646	16.00	4.000	99999
$Ti^{4+} - O^{2-}$ [25]	5111.7	0.2625	0.000	−0.100	314.0
$Sn^{4+} - O^{2-}$ [26]	1414.32	0.3479	13.66	4.000	99999
$Zr^{4+} - O^{2-}$ [25]	985.869	0.3760	0.00	1.350	169.617
$Ce^{4+} - O^{2-}$ [25]	1986.83	0.3511	20.40	7.700	291.75
Three-body $[\Phi_{ijk}(r_{ij}) = \frac{1}{2}K_{ijk}(\theta - \theta_0)^2]$					
Bonds		k (eV·rad^{-2})		θ_0 (deg)	
$O^{2-} - Si^{4+} - O^{2-}$ [21]		2.09724		109.47	

Table 2. Calculated structural parameters and corresponding experimental values [33] reported for orthorhombic ($Cmc2_1$) Li_2SiO_3.

Parameter	Calc	Exp [33]	$\|\Delta\|$(%)
a (Å)	9.5046	9.3960	1.16
b (Å)	5.4464	5.3960	0.93
c (Å)	4.6808	4.6610	0.43
$\alpha = \beta = \gamma$ (°)	90.0	90.0	0.00
V ($Å^3$)	242.31	236.32	2.54

Table 3. Calculated Li-Li separations and activation energies using classical pair-potential method for the lithium ion migration between two adjacent Li sites (refer to Figure 3).

Migration path	Li-Li separation (Å)	Activation energy (eV)
A	2.86	0.21
B	2.90	0.44
C	3.03	0.66
D	3.43	1.26

Table 4. Possible long-range Li ion diffusion paths and their corresponding overall activation energies.

Long-range path	Overall activation energy (eV)
A→A→A→A	0.21
B→A→A→ B	0.44
C→C→C→C	0.66
D→C→D→C	1.26

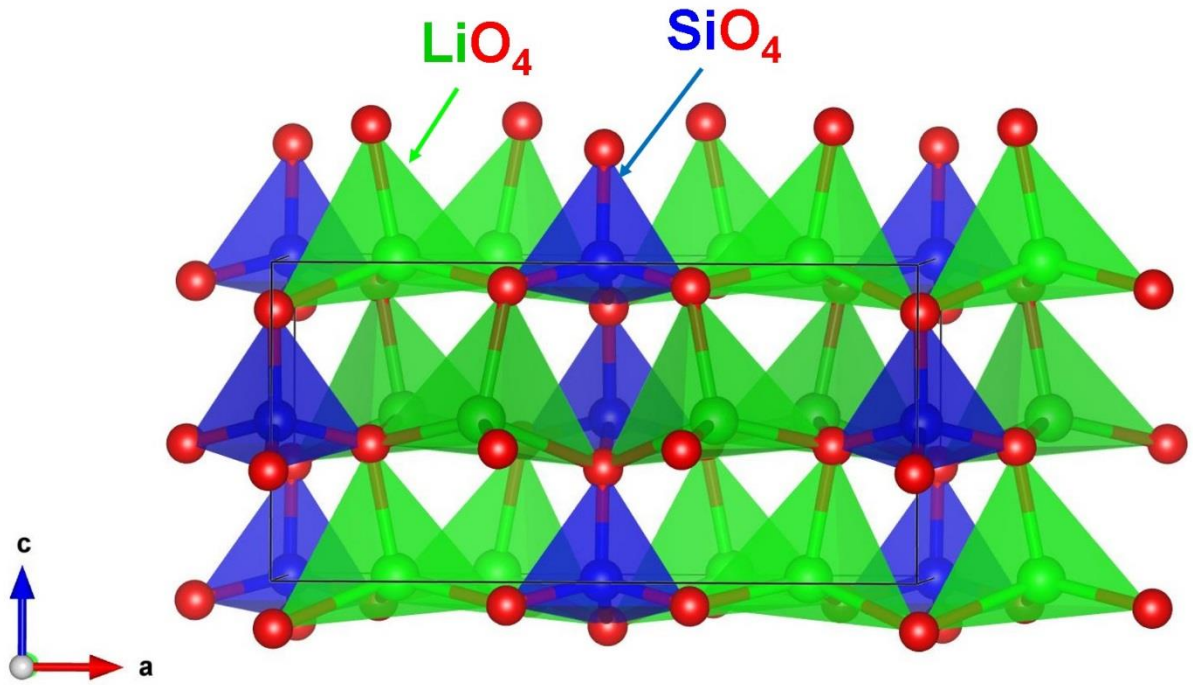

Figure 1. Crystal structure of Li_2SiO_3 (space group $Cmc2_1$).

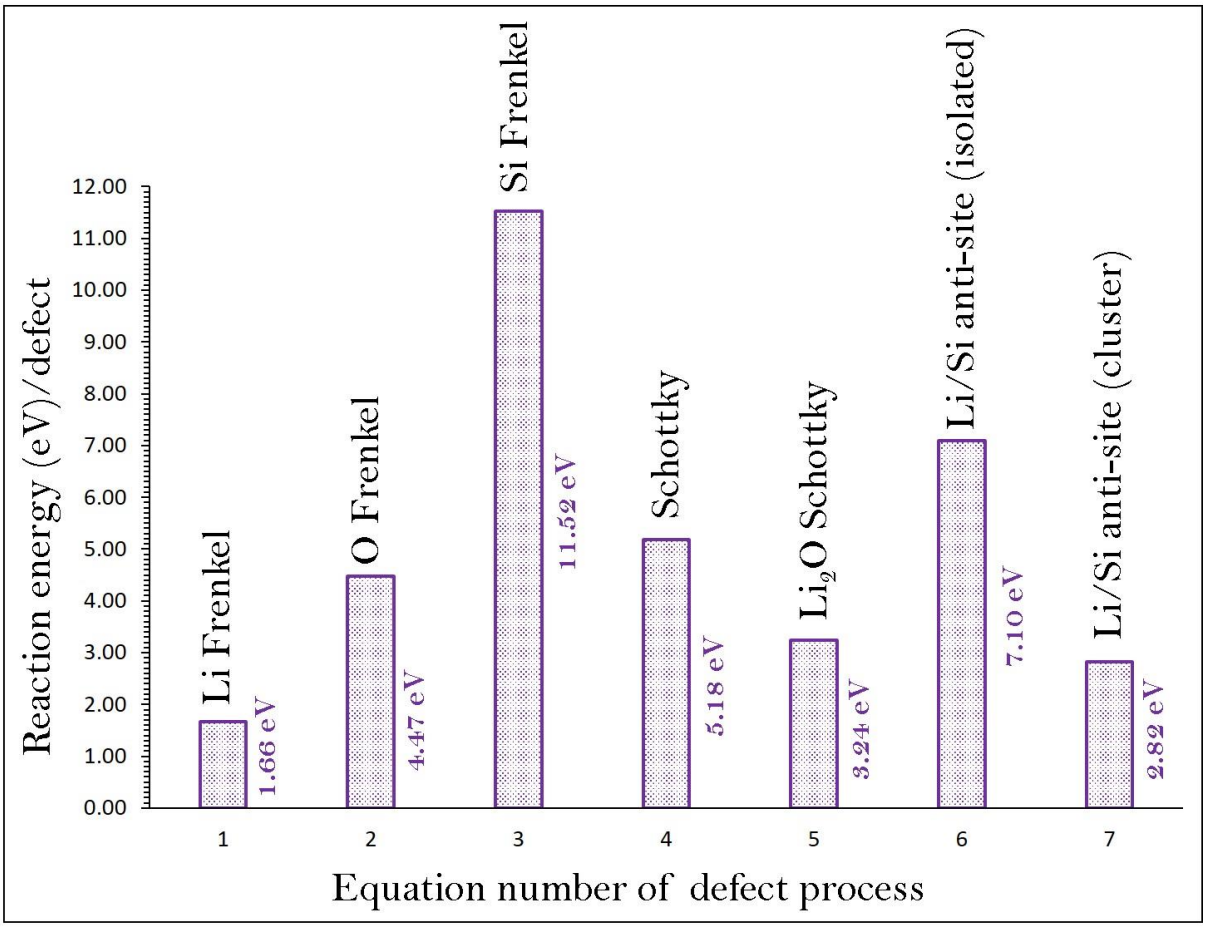

Figure 2. Energetics of intrinsic defect process calculated in orthorhombic Li_2SiO_3.

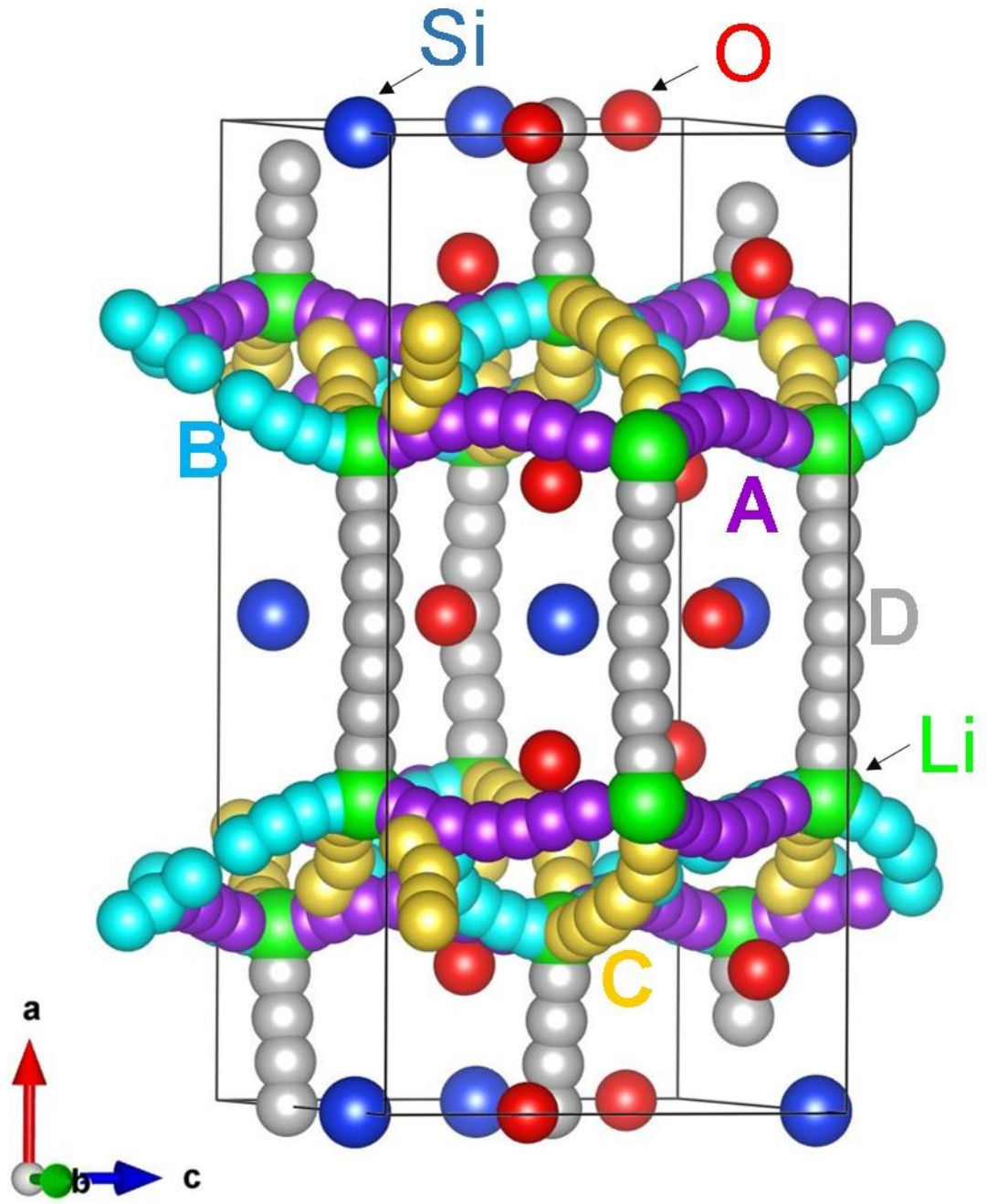

Figure 3. Possible long-range lithium vacancy migration paths considered. Yellow, light blue, grey and purple color atoms correspond to different Li hopping trajectories.

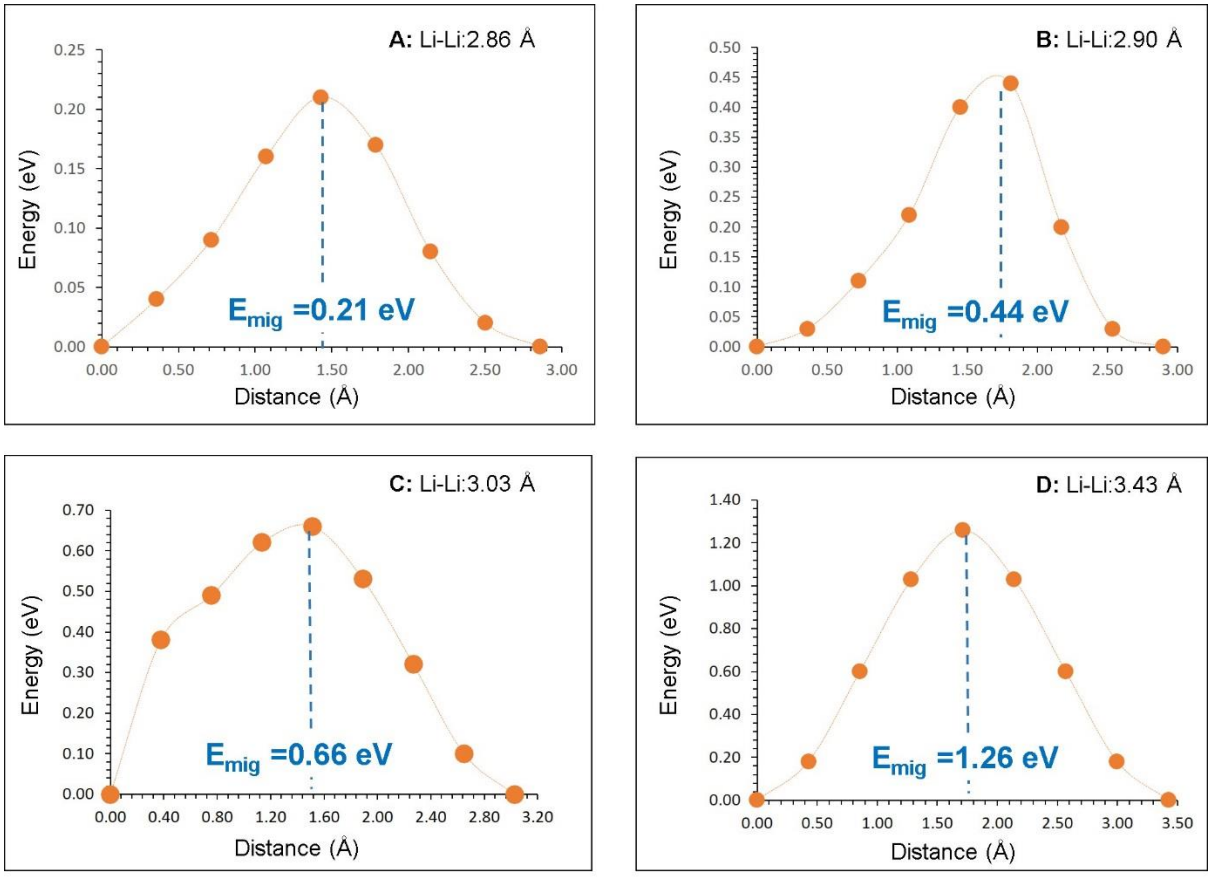

Figure 4. Four different energy profiles [as shown in Figure 3] of Li vacancy hopping between two adjacent Li sites in Li_2SiO_3.

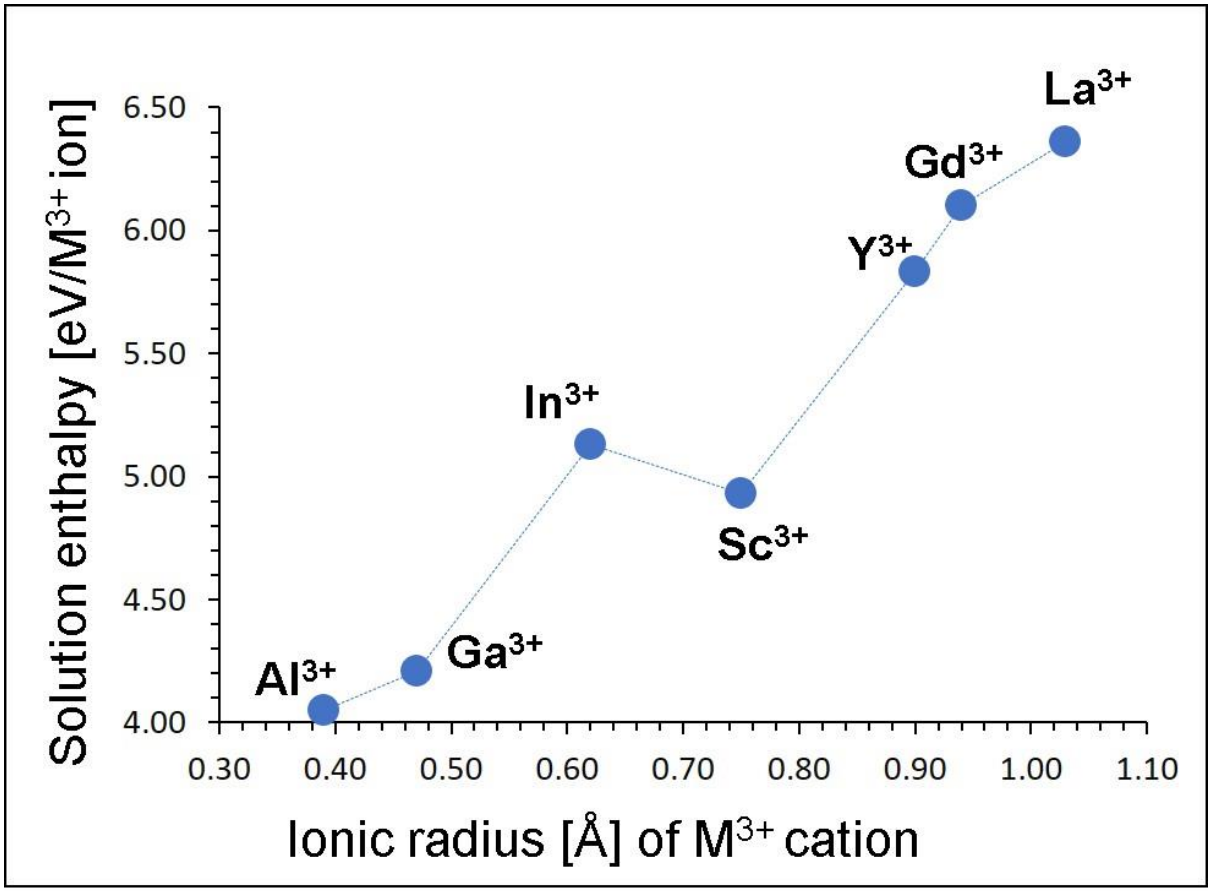

Figure 5. Enthalpy of solution of R_2O_3 (R = Al, Ga, Sc, In, Y, Gd and La) with respect to the R^{3+} ionic radius in Li_2SiO_3.

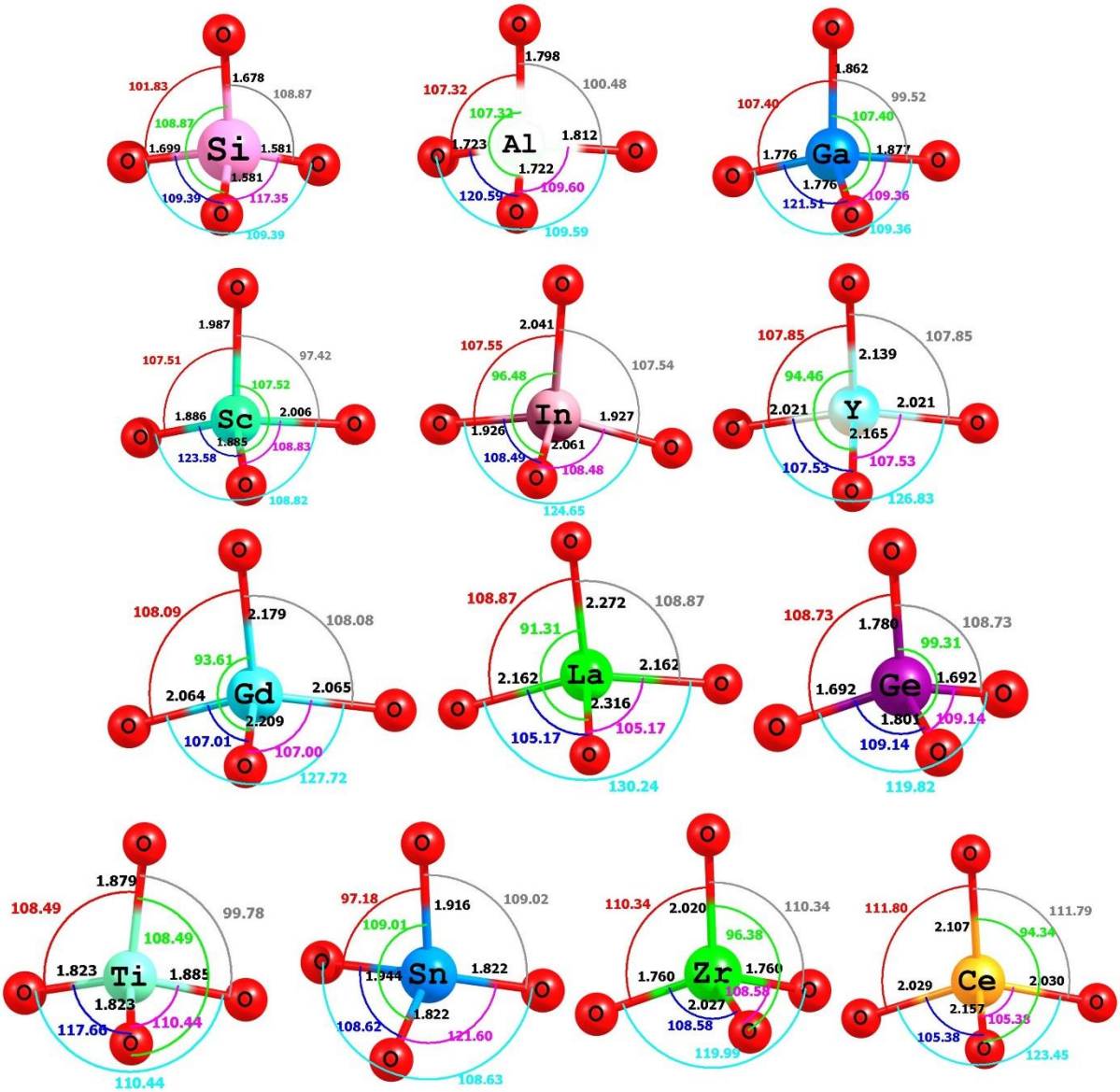

Figure 6. Tetrahedral SiO_4 unit in the relaxed structure of undoped Li_2SiO_3 and the coordination formed by the trivalent (Al, Ga, In, Sc, Y, Gd, and La) and tetravalent (Ge, Ti, Sn, Zr and Ce) dopants on the Si site with neighbour oxygen.

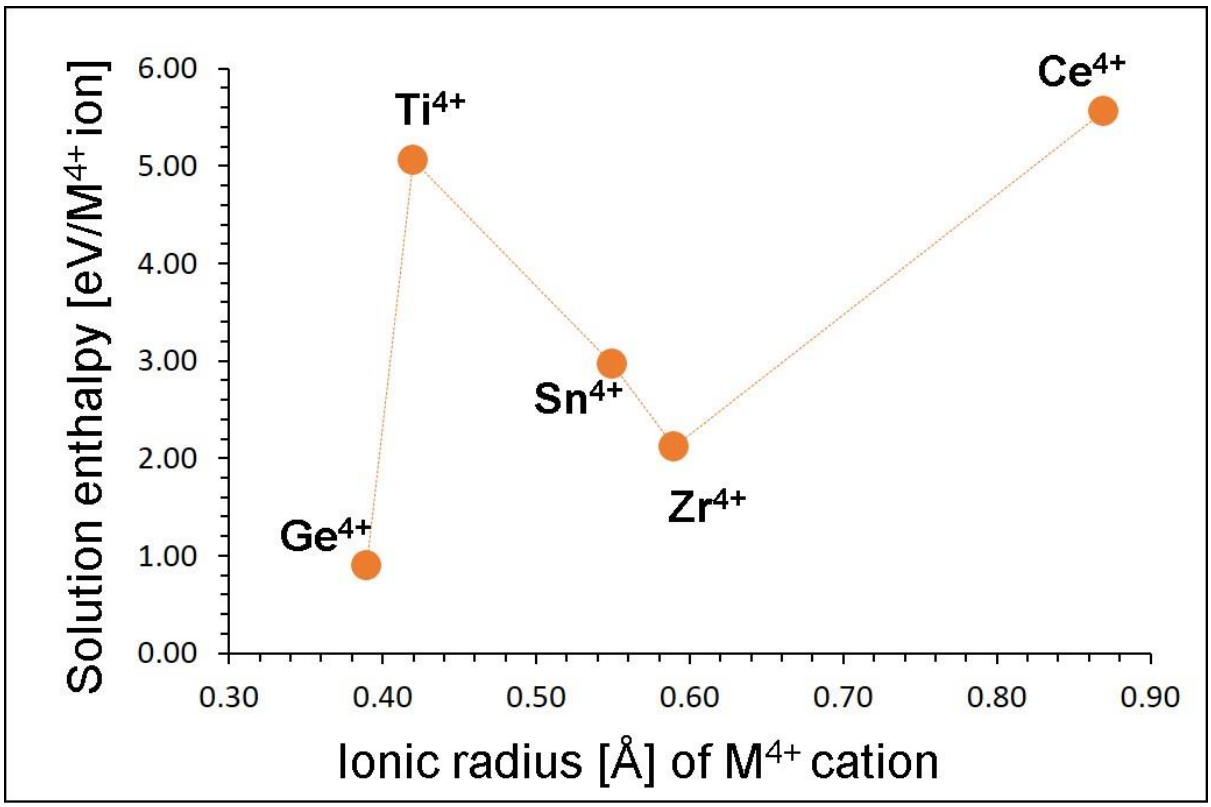

Figure 7. Enthalpy of solution of RO_2 (R = Ge, Ti, Sn, Zr and Ce) with respect to the R^{4+} ionic radius in Li_2SiO_3.